Simulations of Diabetic and Non-Diabetic Peripheral Nerve Myelin Lipid Bilayers

Yiding Yuan[1], Yalun Yu[2], and Jeffery B. Klauda[1,2*]

[1]Department of Chemical and Biomolecular Engineering, [2]Biophysics Graduate Program, University of Maryland, College Park, MD 20742, USA

*Corresponding Author: jbklauda@umd.edu

Abstract:

The multilayered myelin sheath is a critical component of both central and peripheral nervous systems, forming a protective barrier against axonal damage and facilitating the movement of nervous impulses. It is primarily composed of cholesterol (CHL1), phosphatidylcholine (PC), phosphatidylethanolamine (PE), phosphatidylserine (PS), phosphatidylinositol (PI), sphingo-myelin (SM), and galactosylceramide (GalCer) lipids. For rat sciatic nerve myelin (part of the peripheral nervous system, PNS), it has been found that cholesterol and unsaturated fatty acid content are significantly lower in diabetic compared to non-diabetic conditions. In this study, lipid compositions from experimental data are used to create four model rat sciatic nerve myelin lipid bilayers: PI-containing (non-diabetic and diabetic) and PS-containing (non-diabetic and diabetic), which were then simulated using the all-atom CHARMM36 force field. Simulation results of diabetic membranes indicate less rigid, more laterally expansive, and thinner bilayers as well as potentially reduced interactions between GalCer on opposing myelin leaflets, supporting a direct role of cholesterol content decrease in instigating myelin deterioration and diabetic peripheral neuropathy. Compared to PI-lipids, PS-lipids were found to cause higher inter-lipid spacing and decreased order within membranes as a result of their smaller headgroup size and higher inter-lipid hydrogen bonding potential, which allow them to more frequently reside deeper in the membrane plane and produce pushing effects on other lipids. GalCer deuterium order parameters and non-diabetic headgroup-to-headgroup bilayer thicknesses were compared to experimental data, exhibiting close alignment, supporting the future usage of these models to study the PNS myelin sheath.

1. Introduction

Nervous axons are ensheathed by spirals of oligodendrocyte and Schwann cells in the central (CNS) and peripheral (PNS) nervous systems respectively, with their plasma membranes forming the insulating structure known as the myelin sheath.[1] The myelin sheath is a crucial nervous component, serving a dual purpose of promoting nerve impulse conduction and protecting against axonal damage.[2] In biological membranes, lipid composition has been shown to affect an assortment of properties ranging from the mechanical properties and function of the lipid membrane itself to proper folding of related proteins, and the myelin sheath is no different, with deficiencies of glycosphingolipids having been demonstrated to affect membrane fluidity, permeability, and packing.[3-6] Molecular dynamics (MD) simulations can be used to probe the influences of lipid diversity in biological membrane structure and function with atomistic resolution in addition to *in-vitro* experimentation. In recent years, MD simulations have enabled the study of various membranes with complex lipid compositions, including yeast, *E. Coli*, soybean, and *P. Aeruginosa*.[7-10] The CNS myelin sheath has been modeled in a recent study with five different lipid components, but to our knowledge, there has not yet been extensive work done on the PNS myelin sheath.[11]

Diabetic peripheral neuropathy (DPN) refers to the nerve dysfunction that occurs in diabetic individuals, frequently leading to pain, sensory loss, and other malaises.[12] As a protector of the nerve itself, myelin sheath damage often occurs before reaching DPN.[13-14] Although the mechanisms leading to DPN remain obscure, an altered myelin lipid composition has been reported by Cermenati et al. in the sciatic nerves of diabetic rats as a result of decreased levels of sterol-regulatory element binding factor-1c and expression of relevant genes in fatty acid synthesis.[15-16] MD simulations of complex models based on both diabetic and non-diabetic myelin membranes could provide further insight from a biophysical perspective into the relation between myelin lipid composition and DPN.

Interestingly, Cermenati et al. also reported a higher phosphatidylinositol (PI) component in their myelin compared to phosphatidylserine (PS), which is the reverse from the norm in studies on rat sciatic nerve myelin, as well as human PNS myelin.[17-19] Both PI and PS lipids play crucial roles in cellular function, with the former in phosphorylated form (phosphoinositides) notable for their exigency in the signal transduction pathway, and the latter important markers for apoptosis and blood clotting.[20-22] MD simulations of complex model membranes containing either PI or PS-

lipid would enable greater understanding of the roles of each lipid in membrane structure and function.

In this study, we present MD simulations of four complex model membranes representing PI-lipid-containing non-diabetic and diabetic myelin bilayers, and PS-lipid-containing non-diabetic and diabetic myelin bilayers. Compositions are estimated from data reported in several experimental studies.[15, 17-18] After 400 ns and 600 ns of simulation, respectively, for the diabetic and non-diabetic models, a variety of properties are calculated for each model and compared to the others, and for some select properties, to experimental figures. Our overall goals are as follows: to study the effects of lipid composition changes in diabetes as well as PI vs. PS-lipid inclusion on the structural and dynamical properties of the PNS myelin sheath, and to provide a realistic representation of the PNS myelin sheath. Although this work is not a fully comprehensive model of the PNS myelin sheath, lacking components such as membrane asymmetry, crucial myelin proteins, gangliosides, and multiple layers, we believe that it supplies a reasonable starting point for further simulation studies involving PNS myelin.[23-25]

2. Methods

2.1 Model and System Setup

The primary basis of our models is Cermenati et al.'s electrospray mass ionization experiment on sciatic nerve myelin sheath lipid compositions in non-diabetic and streptozotocin-induced diabetic Sprague-Dawley rats.[15] Here (see Figure 1 in reference 15), the following composition data are provided separately from one another for both diabetic and non-diabetic conditions: fractions of individual lipid types (phosphatidylethanolamine (PE), phosphatidylcholine (PC), phosphatidylserine (PS), phosphatidylinositol (PI), sphingomyelin (SM), unidentified glycosphingolipid, and sulfatides) relative to their total, fraction of cholesterol relative to the total myelin, fractions of individual fatty acid tails (e.g. 18:0/stearic acid tails) relative to the total myelin, and fractions of specific FA pairings associated with different phospholipids (e.g. 20:4/18:2 PC—2-arachidonyl-3-linoleoyl-D-glycero-1-phosphatidylcholine, ALPC). Individual lipid fractions are compared to older studies on healthy rats in **Table S1**.[17-18] The phospholipid compositions are in general agreement with the other works, except for the reported higher PI fraction relative to PS, which is also dissimilar to findings from studies on human peripheral nerve myelin.[19] From its presence in other studies, the presence of sulfatides

(sulfated galactosylceramides), and its noteworthy prevalence in myelin, the unidentified glycosphingolipid is determined to be primarily galactosylceramide (GalCer).[26]

In order to investigate the effects of both diabetes and PS/PI-lipid content on myelin bilayers, four models with different lipid compositions were created: PI-containing/non-diabetic, PI-containing/diabetic, PS-containing/non-diabetic, and PS-containing/diabetic. Realistic fractions of general lipid types were estimated from literature figures and are compared to model fractions in **Figure S1**. Relative ratios of cholesterol to phospholipid were not reported by Cermenati et al., so possible non-diabetic cholesterol fractions were calculated from figures reported in older works, and each were decreased by ~60% in accordance with Cermenati et al. for diabetic fractions. Non-sterol lipid fractions were determined based on adjusting Cermenati et al.'s reported lipid fractions for diabetic and non-diabetic to their respective cholesterol fractions, and model fractions were assigned close to these. Lipid types with prevalence <5%, such as sulfatides and PS or PI-lipids in PI and PS-containing models respectively, were removed, leaving glycosphingolipid (GalCer), PC, PE, PI *or* PS, and SM categories extant for all models. Fatty acid tails were assigned based on Cermenati et al.'s figures for individual tail fractions (**Figure S2**), in addition to select notable pairings reported. GalCer was modeled as d18:1/16:0 GalCer to account for both 16:0 and 18:1 GalCer being listed. 20:4/18:2 PC (ALPC) and 18:1/18:1 PS (2,3-dioleoyl-D-glycero-1-phosphatidylserine— DOPS) were also included to match notable fatty acid pairings. Although there are some differences between model and calculated experimental lipid and fatty acid tail compositions, such as ~25% lower 18:0 tail count in the models, model lipid compositions should be in the reasonable range of real-world physiological variation. The fraction of 20:4 tails is significantly higher than experimental values, but this helps account for the additional small proportions of polyunsaturated fatty acid tails (18:3 and 22:6), as well as the proportion of additional longer tails (of 20 carbons or longer) not included elsewhere in the model.

The CHARMM-GUI *Membrane Builder* is used to build each of the model lipid bilayers, all of which possess the same lipid composition in both leaflets and are fully hydrated with at least 50 water molecules per lipid.[27-30] The exact makeup of each model membrane is shown in **Table 1**. Cumulatively, the most notable differences between non-diabetic and diabetic models are that diabetic models have significantly lower cholesterol and higher saturated fatty acid chain content (**Figure S2**). Between PI and PS-containing models, differences in composition are small except for the inclusion of PI and PS-lipids respectively. Each model is built in triplicate, with each replica

generated separately, resulting in different starting trajectories and lipid placements within the bilayer.

Table 1. Exact lipid composition of all model membranes per leaflet and proportions of saturated/unsaturated lipid tails. CHL1: cholesterol, GalCer: galactosylceramide— (d18:1/16:0 ceramide + β-galactose), DOPC: 2,3-dioleoyl-D-glycero-1-phosphatidylcholine, ALPC: 2-arachidonyl-3-linoleoyl-D-glycero-1-phosphatidylcholine, SLPE: 1-Stearoyl-2-Linoleoyl-Phosphatidylethanolamine, SLPI: 1-stearoyl-2-linoleoyl-sn-glycero-3-phosphoinositol, SSM: d18:1/18:0 sphingomyelin, SLPS: 1-Stearoyl-2-Linoleoyl-Phosphatidylserine, DOPS: 2,3-dioleoyl-D-glycero-1-phosphatidylserine, DSPC: 2,3 distearoyl-D-glycero-1-Phosphatidylcholine, SOPE: 1-Stearoyl-2-Oleoyl-Phosphatidylethanolamine, DSPE: 2,3-distearoyl-D-glycero-1-Phosphatidylethanolamine

Lipid	**PI-Containing, Non-Diabetic**	**PS-Containing, Non-Diabetic**	**PI-Containing, Diabetic**	**PS-Containing, Diabetic**
CHL1	36	37	13	14
(18:1/16:0) GalCer	20	20	21	21
(18:1/18:1) DOPC	7	5		
(18:0/18:0) DSPC			13	6
(20:4/18:2) ALPC	5	6	7	12
(18:0/18:1) SOPE			7	
(18:0/18:0) DSPE				16
(18:0/18:2) SLPE	11	11	6	
(18:0/18:2) SLPI	13		19	
(18:0/18:2) SLPS		8		14
(18:1/18:1) DOPS		5		5
(18:1/18:0) SSM	8	8	13	12
Total lipid/leaflet	100	100	100	100
Proportion of unsaturated tails	0.59	0.63	0.47	0.46
Proportion of saturated tails	0.41	0.37	0.53	0.54

ALPC and SLPI lipids were not available in CHARMM-GUI at the time of setup (however, SLPI is now present), so they were created by substituting 2,3-diarachidonyl-D-glycero-1-phosphatidylcholine (DAPC) and 1,2-dilinoleoyl-sn-glycero-3-phosphoinositol (DLiPI) as initial placeholders, and then mutating them to ALPC and SLPI respectively through CHARMM. **Figure 1** includes the chemical structures of these lipids along with snapshots of the end-of-simulation membranes.

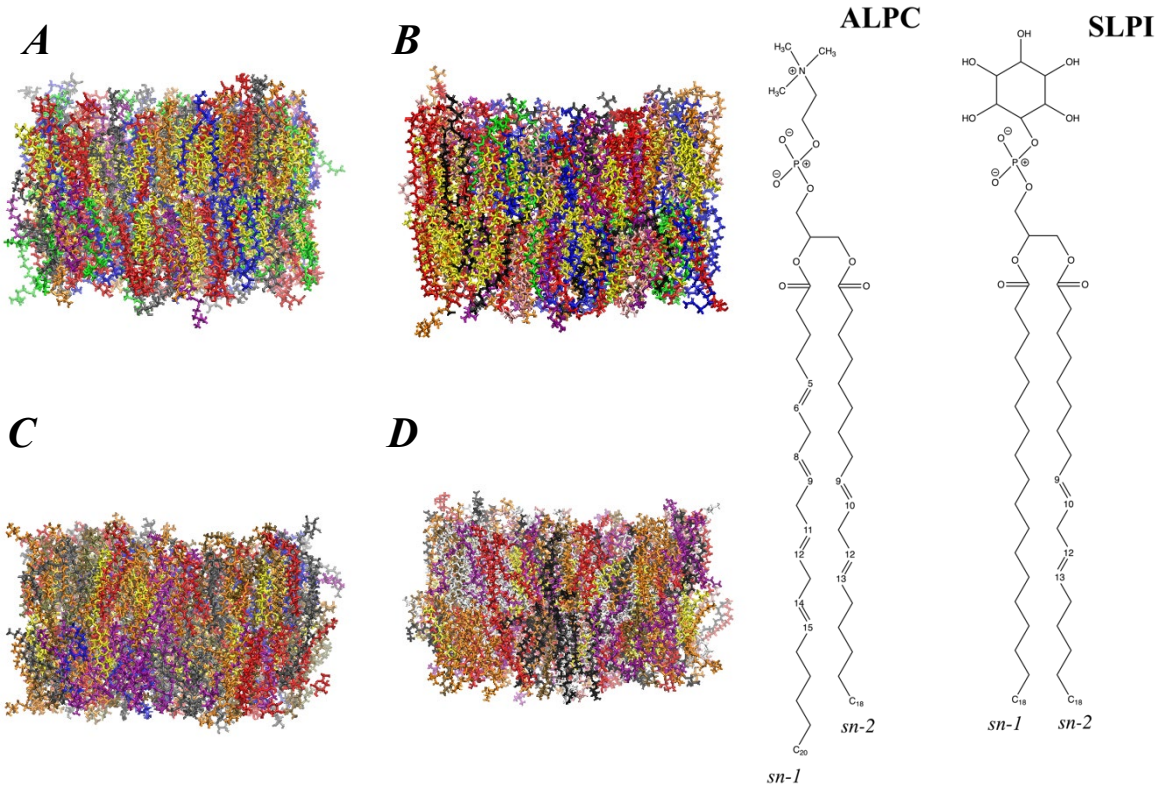

Figure 1. The left image includes snapshots of all membranes (A— PI-containing, non-diabetic; B— PS-containing, non-diabetic; C— PI-containing, diabetic; D— PS-containing, diabetic) at end of simulation. CHL1 in yellow, GalCer in red, DOPC in green, ALPC in purple, DSPC in ochre, SLPE in blue, DSPE in white, SLPI in gray, SLPS in black, DOPS in pink, SSM in orange, SOPE in tan. The right image includes chemical structures of ALPC and SLPI.

2.2 Simulation

After system setup and input file generation in CHARMM-GUI, equilibrium and production runs were simulated using NAMD coupled with the CHARMM36 (C36) lipid force field and the modified TIP3P water model.[31-34] Equilibrium runs followed the standard CHARMM-GUI six-step procedure, and production runs continued for 400 ns and 600 ns for all diabetic and all non-diabetic models, respectively, using a timestep of 2 fs and data output every 5 ps.[27] Based on the average male Sprague-Dawley rat body temperature of 37 °C, which is also within healthy physiological range for humans, all simulations were performed using the isothermal-isobaric (NPT) ensemble at a constant temperature of 310.15 K, maintained through Langevin dynamics, and a constant pressure of 1 bar, maintained through the Nosé-Hoover-Langevin piston.[35-37] Hydrogen atoms were constrained with the SHAKE algorithm.[38] For long-range electrostatic interactions, the Particle Mesh Ewald fast Fourier transform with an

interpolation order of 6 and a direct space tolerance of 10^{-6} was used.[39] van der Waals interactions were switched off between 8 and 12 Å by the Lennard-Jones potential with a force-based switching function.[40] Simulation movies of one replicate of each model for both the top and bottom membranes can also be found in the supplementary materials section.

2.3 Analysis

Analysis for all model membranes was based on the last 150 ns of production run (250-400 ns and 450-600 ns for diabetic and non-diabetic models, respectively). Properties computed include overall surface area per lipid (SA/lipid), area compressibility modulus (K_A), component SA/lipid, acyl chain deuterium order parameters (S_{CD}), electron density profiles (EDP), bilayer thicknesses, chain interdigitation, two-dimensional radial distribution functions (2D-RDF), hydrogen bonding, and tilt angles. Prior to other analyses, system equilibration and convergence between replicates were confirmed for at least the final 150 ns based on examination of the overall SA/lipid trend over time. Reported figures are the average of all three replicates for the given model. All figures were created in gnuplot or MATLAB ver. R2019B, and snapshots of membrane lipids are taken in the Visual Molecular Dynamics (VMD) program.[41-42] Data from literature figures in cases where exact numbers were not provided were pulled using the WebPlotDigitizer application.[43]

The overall SA/lipid was obtained by simply dividing the area of the simulation box by the number of lipids per leaflet. From this figure, the area compressibility modulus was computed with the equation:

$$K_A = \frac{k_B T \langle A \rangle}{N \sigma^2_{\langle A \rangle}} \quad (1)$$

where k_B, T, $\langle A \rangle$, N, and $\sigma_{\langle A \rangle}$, stand for the Boltzmann's constant, the absolute temperature, the average overall SA/lipid, and variance of the average SA/lipid, respectively. Component SA/lipid was obtained using the *X*-*Y* coordinates of representative atoms (O3 in sterols, C2 in glycerophosphates, and C2S in sphingolipids) for each individual lipid of the primary cell. Then, the primary cell and eight surrounding images were imported into Qhull to construct complex polygons for each atom, from which the total polygon area for each lipid type is extracted and averaged to obtain the component surface areas.[44] S_{CD}'s were calculated using the formula:

$$S_{CD} = \left| \left\langle \frac{3}{2} cos^2\theta - \frac{1}{2} \right\rangle \right| \quad (2)$$

where θ refers to the instantaneous angle between the vector of the C-H bond and the bilayer normal. In experiments, hydrogen is replaced by deuterium, but we are reporting this with our systems containing hydrogen as there is little influence on the properties.

The EDP's were obtained through first recentering the bilayer at $Z = 0$ so that there was symmetrical distribution around the membrane center, and then calculating the densities for each atom, which were combined to acquire both component and total density profiles. From these profiles, the headgroup-to-headgroup distance, D_{HH} (distance between the peaks in the total EDP), the overall bilayer thickness, D_B (distance between the half maximum positions in the water-only EDP), and the hydrophobic distance, $2D_C$ (distance between the half maximum positions in the hydrophobic tail EDP) were acquired. Furthermore, by computing the EDP's for top and bottom leaflets only, the following equation was used to calculate interdigitation:

$$\lambda_{ov} = \int_{-L}^{+L} 4 \frac{\rho_t(z) \times \rho_b(z)}{(\rho_t(z) + \rho_b(z))^2} dz \quad (3)$$

where λ_{ov}, $\rho_t(z)$, $\rho_b(z)$, and $[-L, L]$ are respectively the parameter measuring degree of interdigitation, the densities of the top and bottom leaflets at distance z from the bilayer center, and the region along the z-axis where $\rho_t(z)$ or $\rho_b(z) \neq 0$. [45]

2D-RDF's were determined based on the coordinates of P for glycerophospholipids, O3 for sterols, and C2S for sphingolipids (**Figure 2**). The number of hydrogen bonds was counted based on the definition that a hydrogen bond contains a proton-acceptor pair distance less than 2.4 Å and an angle greater than 150°.

Tilt angles were determined for phospholipid headgroups, sterol, and β-galactose as the angle between a vector created by two representative atoms and the bilayer normal. The following were the representative atoms used for cholesterol, β-galactose, and the PI, PS headgroups respectively: C3 → C17, O1 → O4, P → C14, and P → N. The structures of these headgroups, as well as positions of these atoms are also shown in **Figure 2**.

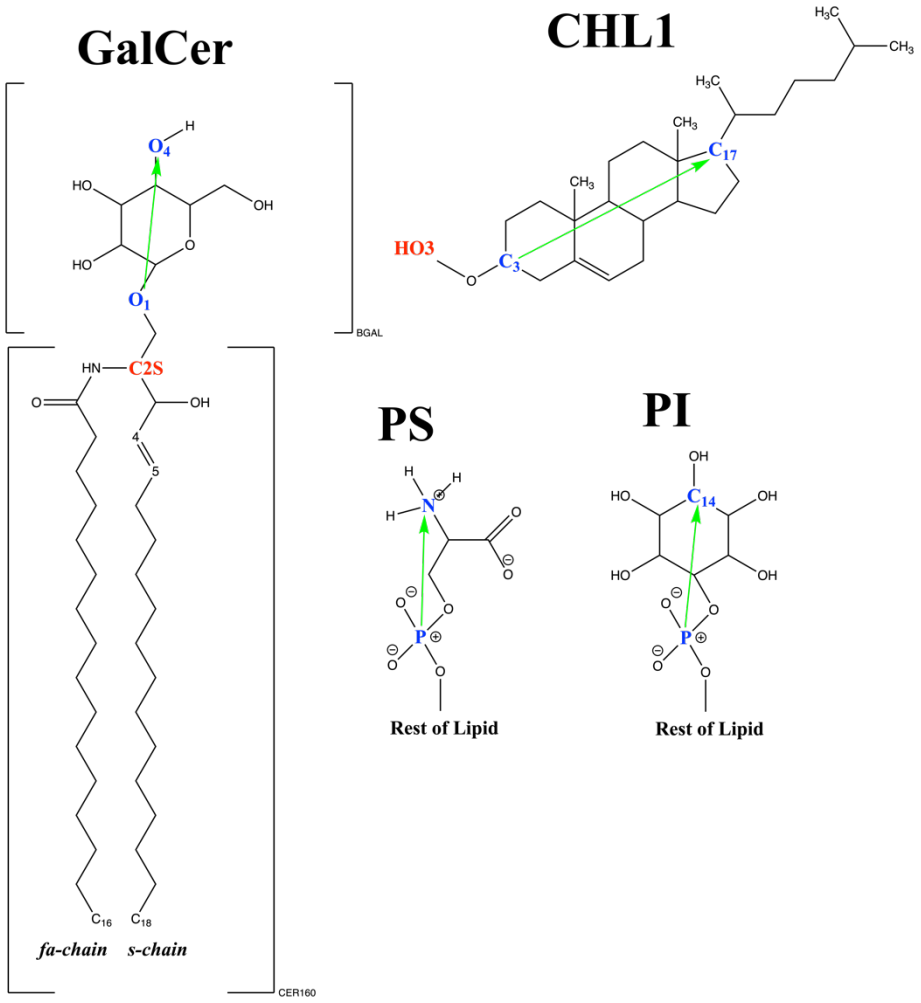

Figure 2. Structures of GalCer and CHL1, as well as the PS and PI-lipid headgroups are provided. Atoms used for tilt angle vectors are marked in blue, with the arrow pointing in the direction of the vectors. Blue phosphates are also used in the calculation of S_{CD}'s. Other S_{CD} reference atoms are marked in red.

3. Results

3.1 Surface Area (Sa/lipid), Area Compressibility Modulus (K_A), and Deuterium Order Parameters (S_{CD})

The overall SA/lipid is a good measure of lipid packing within the membrane, and its trend over time demonstrates when the simulation reaches equilibrium. A plot of overall SA/lipid over time is provided at **Figure S3**, where it is visible that all simulations reach equilibrium and good convergence between the triplicates with different initial lipid placements and velocities by at least 150 ns prior to the run's finish (before 250 ns and 450 ns respectively in diabetic and non-diabetic

models), justifying further analysis using the final 150 ns of simulation in each model. **Table 2** shows the average overall SA/lipid and K_A for all models studied. The overall SA/lipid is significantly higher in both diabetic models compared to their non-diabetic counterparts, with a corresponding lower K_A, indicating that lipids are not packed as tightly together, and that the membrane as a whole is less rigid in diabetic conditions. Cholesterol is a rigid component that decreases membrane fluidity, so these differences can be attributed to the comparatively lower cholesterol proportions in diabetic membranes. This is in spite of the lower unsaturated fatty acid proportion, demonstrating cholesterol's more prominent role in modulating membrane properties. Between PS and PI-containing models of the same disease condition, however, an interesting trend arises of slightly higher overall SA/lipid in the PS-containing models. The diabetic SA/lipid are statistically the same, with a P-value of 0.19 from a paired two-sample *t*-test, but this trend is consistent between all models.

Table 2. SA/lipid and K_A for all models. Errors are standard errors (SE) from the three replicates.

	Average SA/lipid ($Å^2$) ± SE	**Average K_A (N/m) ± SE**
PI-Containing, Non-Diabetic	47.66 ± 0.12	0.42 ± 0.03
PS-Containing, Non-Diabetic	48.24 ± 0.08	0.45 ± 0.02
PI-Containing, Diabetic	58.51 ± 0.24	0.20 ± 0.01
PS-Containing, Diabetic	59.08 ± 0.37	0.19 ± 0.01

The component SA/lipid is helpful for comparing packing between different lipid types in a mixed bilayer, and values for all lipid types are presented in **Table 3**. For each model, CHL1 area is at ~30 $Å^2$ with small variation, as is expected given its rigid ring structure. Outside of CHL1, ALPC, SSM, and CER160 component SA/lipid can be compared between models as these lipid types are universally present. Notably, their component SA/lipid is significantly higher in the diabetic models, aligning to the previous trend with overall SA/lipid. Again, as with the overall SA/lipid, there is a consistent trend of slightly higher surface areas in PS-containing models for the same lipid type and disease condition. (such as 58.9 vs. 56.3 $Å^2$ in PS-containing, diabetic vs. PI-containing, diabetic CER160).

Table 3. Component SA/lipid for all lipids. Errors are standard errors (SE) from the three replicates.

	PI-Containing, Non-Diabetic	PS-Containing, Non-Diabetic	PI-Containing, Diabetic	PS-Containing, Diabetic
Lipid	**Area ($Å^2$) ± SE**	**Area ($Å^2$) ± SE**	**Area ($Å^2$) ± SE**	**Area ($Å^2$) ± SE**
CHL1	29.7 ± 0.4	30.4 ± 0.4	31.5 ± 1.5	30.0 ± 1.0
GalCer	53.1 ± 0.8	54.0 ± 0.7	56.3 ± 1.9	58.9 ± 0.9
DOPC	62.1 ± 1.5	62.2 ± 1.7		
DSPC			65.0 ± 1.6	63.9 ± 1.6
ALPC	63.7 ± 1.6	65.2 ± 1.9	69.0 ± 2.5	70.3 ± 1.8
SOPE			65.4 ± 2.7	
DSPE				65.3 ± 1.6
SLPE	61.1 ± 1.6	61.7 ± 1.2	66.2 ± 2.2	
SLPI	61.0 ± 0.9		65.6 ± 1.3	
SLPS		61.2 ± 1.3		67.7 ± 1.9
DOPS		62.5 ± 2.0		67.4 ± 2.1
SSM	54.0 ± 1.0	54.8 ± 1.1	59.3 ± 1.4	60.4 ± 1.2

S_{CD}'s provide important information on the acyl chain order of the lipid bilayer, with higher values corresponding to greater chain order. **Figure 3** shows the S_{CD}'s for CER160 for all model membranes, and similar figures for CHL1, ALPC, and SSM are contained in **Figure S4**. General profile shapes for S_{CD} are conserved throughout, but chain order trend noticeably lower in diabetic membranes. This corresponds well to the general cholesterol modulated trend noted in SA/lipid—with lower proportions of these rigid components, there is decreased chain order. In accordance with the previously observed trends with SA/lipid, all lipids demonstrate a trend of slightly decreased chain orders in many carbons for PS-containing models compared to their PI-containing counterparts. For example, compare carbons 6-17 between PS-containing, diabetic, and PI-containing, diabetic models in **Figure 3**'s CER160.

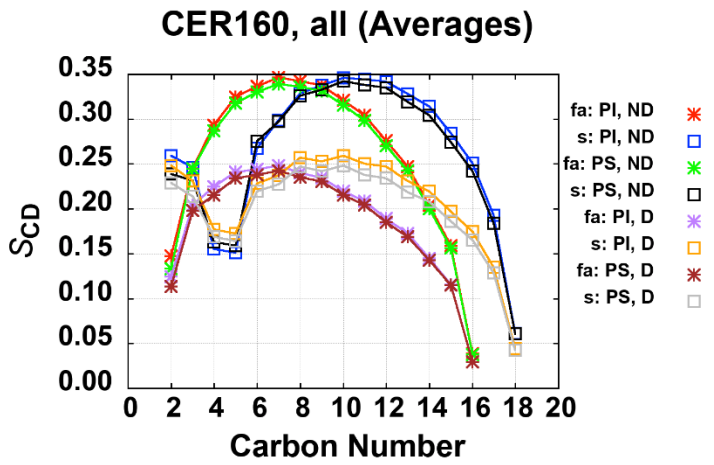

Figure 3. S_{CD}'s for CER160 in all membranes. PI/PS stand for PI and PS-containing, and D/ND stand for diabetic and non-diabetic respectively.

Morrow et al.[46] performed an NMR experiment on GalCer in bilayers composed of 7% GalCer (mixed between 18:0 and 24:0), 70% 1-stearoyl-2-oleoyl-sn-glycero-3-phosphocholine (SOPC) and 23% cholesterol at 40 °C, which is reasonably similar enough in both temperature and composition to the model membranes constructed for comparison. Smoothed monotonically decreasing S_{CD} values for 18:0 *s*-chains in the experimental GalCer are provided to which S_{CD} values (correspondingly arranged in a monotonically decreasing pattern) of the 18:1 sphingosine chain in simulation CER160 are compared in **Figure 4**. Overall, the experimental S_{CD} is noticeably higher than that of the diabetic membranes, converging quite closely to the non-diabetic S_{CD} profile. This is a result of the experimental and non-diabetic membranes being in the same thermodynamic state, as modulated by their shared high cholesterol content. At ~40 °C, membranes typically transition to the liquid-ordered (L_o) state above ~20% cholesterol content — hence, both the experimental 23% cholesterol membrane and the non-diabetic 36-37% cholesterol membrane should be in the L_o state and have similarly high acyl chain order.[47] The diabetic bilayers have lower cholesterol content at 13-14%, and are as such in a different phase from the experimental membrane, with differing acyl chain order correspondingly. As such, the similar S_{CD} between the experimental and non-diabetic bilayers suggests good alignment between simulation and experiment.

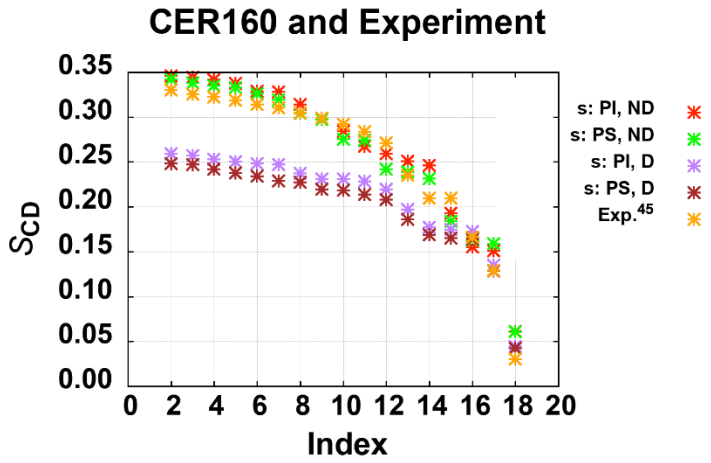

Figure 4. Comparing CER160 *s*-chain S_{CD}'s to experimental S_{CD} index by reducing order.[46] PI/PS stand for PI and PS-containing, and D/ND stand for diabetic and non-diabetic respectively.

3.2 Electron Density Profiles (EDP's), Thicknesses, and Chain Interdigitation

EDP's show the electron density of bilayers from the center to the surrounding water solution and are helpful for analyzing model membrane properties along the *Z*-axis. **Figure 5** compares the overall EDP's of each model system, and **Figure S5** contains component EDP's outlining differences between various groups in each model.

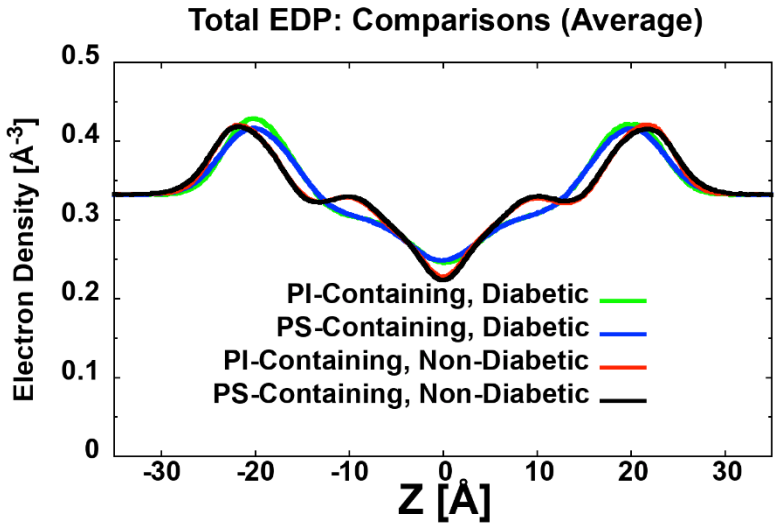

Figure 5. Comparison of total electron density profiles for all model membranes.

The overall EDP's for diabetic and non-diabetic models are visibly different from one another. In both non-diabetic profiles, the minima at $Z = 0$ Å is ~0.03 Å^{-3} lower and the outermost maxima ~2 Å wider than in the diabetic profiles, the latter of which aligns with the increased D_{HH} thickness values shown in **Table 4**. There is also an additional local maximum at $Z = \sim\pm9$ Å in the non-diabetic profiles which is missing in the diabetic. In **Figure S5**, there are notable differences between the carbon profiles in diabetic and non-diabetic models, with the non-diabetic models having higher C (carbons bound to four non-hydrogen atoms) peaks at $Z = \sim\pm12$ Å, CH (methylene) peaks at $Z = \sim\pm10$ Å, a higher CH3 (methyl) peak at $Z = \pm0$ Å, and a lower CH2 (methine) minima at $Z = 0$ Å. This can be explained by the higher cholesterol content in non-diabetic models (**Figure S6**), which contain more CH and CH3, and the subsequently lowered phospholipid content, which contain more CH2. These differences explain the additional local maxima at $Z = \pm\sim9$ Å as well as the lower minima at $Z = 0$ Å in non-diabetic profiles. It is also noticeable that there are slightly higher peaks at $Z = \sim\pm23$ Å in PI-containing models, which can be explained by inositol simply being a larger chemical group with more electrons than serine. This is corroborated by the consistently higher peaks in the same position for inositol compared to serine in **Figure S5**.

Table 4. Thicknesses for each model membrane. D_{HH} is the headgroup-to-headgroup thickness; D_B is the overall bilayer thickness; $2D_C$ is the hydrophobic thickness. Errors are standard errors (SE) from the three replicates.

	D_{HH} (Å) ± SE	D_B (Å) ± SE	$2D_C$ (Å) ± SE
PI-Containing, Non-Diabetic	43.3 ± 0.2	42.4 ± 0.0	32.9 ± 0.0
PS-Containing, Non-Diabetic	43.5 ± 0.2	41.2 ± 0.1	32.8 ± 0.0
PI-Containing, Diabetic	39.7 ± 0.1	40.0 ± 0.2	30.1 ± 0.1
PS-Containing, Diabetic	40.1 ± 0.1	38.8 ± 0.2	30.0 ± 0.1

Corresponding with the noted ~2 Å increase in distance between the overall maxima in **Figure 5**, all thicknesses are ~2-3 Å higher for the non-diabetic models compared to their diabetic counterparts. Due to the lower cholesterol content in diabetic models, individual lipids are laterally spread out farther and less rigid (as evidenced by their heightened SA/lipid and lowered chain order), culminating in decreased vertical leaflet height and overall thickness. The chain interdigitation values in **Table S2** can be also used to help visualize these differences. There is a clear increase in interdigitation with all lipid types in the diabetic models, aligning with their generally lower thicknesses as the opposite lipids are closer together in a more disordered state.

There is also a trend of D_B thicknesses being ~1 Å lower in PS-containing models, which aligns with the slightly increased SA/lipid of PS-containing models. With increased distance between individual lipids, there is more potential for water molecules to penetrate deeper into the membrane, decreasing the water thickness.

The non-diabetic D_{HH} calculated here can also be compared to an X-ray diffraction study performed by Vonasek et al. on rat sciatic nerve myelin sheath membranes.[48] At room temperature, the experimental D_{HH} measured is 47.0 ± 2.0 Å. This is somewhat thicker than the simulated non-diabetic D_{HH} in **Table 4** (43.3 ± 0.2 Å and 43.5 ± 0.2 Å respectively for PI and PS-containing models), but the simulation is set up at a physiological temperature of 37 °C. The exact experimental temperature was not provided but stated to have been done at room temperature; assuming the X-ray diffraction experiment were performed at the common room temperature of ~20 °C, this would be an almost 20 °C increase in temperature from experiment and simulation. As a trend, thickness lowers with increased temperatures, with large D_{HH} decreases in ~1-4 Å having been recorded for 20 °C increases in simulations of pure saturated lipids.[49] Taking an expected similar temperature fluctuation into account for the experimental D_{HH}, the experimental D_{HH} at physiological temperature would decrease to then be within standard error range of the simulated values, demonstrating good alignment between simulation and experiment.

3.3 Tilt Angles

The tilt angle distributions of PI (from SLPI) and PS (from SLPS and DOPS), CHL1, and BGAL in GalCer were computed and can be used to quantify the spatial orientations of these lipid headgroups within the model membranes. **Figure 6** compares tilt angles for BGAL in all models, and **Figure S7** contains similar graphs for CHL1, PI, and PS. CHL1 is less upright in diabetic membranes, with a higher tilt angle distribution, which corresponds to the higher SA/lipid allowing it more space to angle itself than the tightly packed non-diabetic system. Inositol and serine differ greatly in structure from each other, with inositol being larger, as well as in interaction potential (inositol has five hydroxyl groups, indicating greater ability for acting as the donor in hydrogen bonds), but PI and PS tilt angle distributions are quite similar to one another, especially in the diabetic models, where differences are little to none. BGAL shows noticeable differences across all models, with higher angle distributions for diabetic models, as well as for PI-containing models.

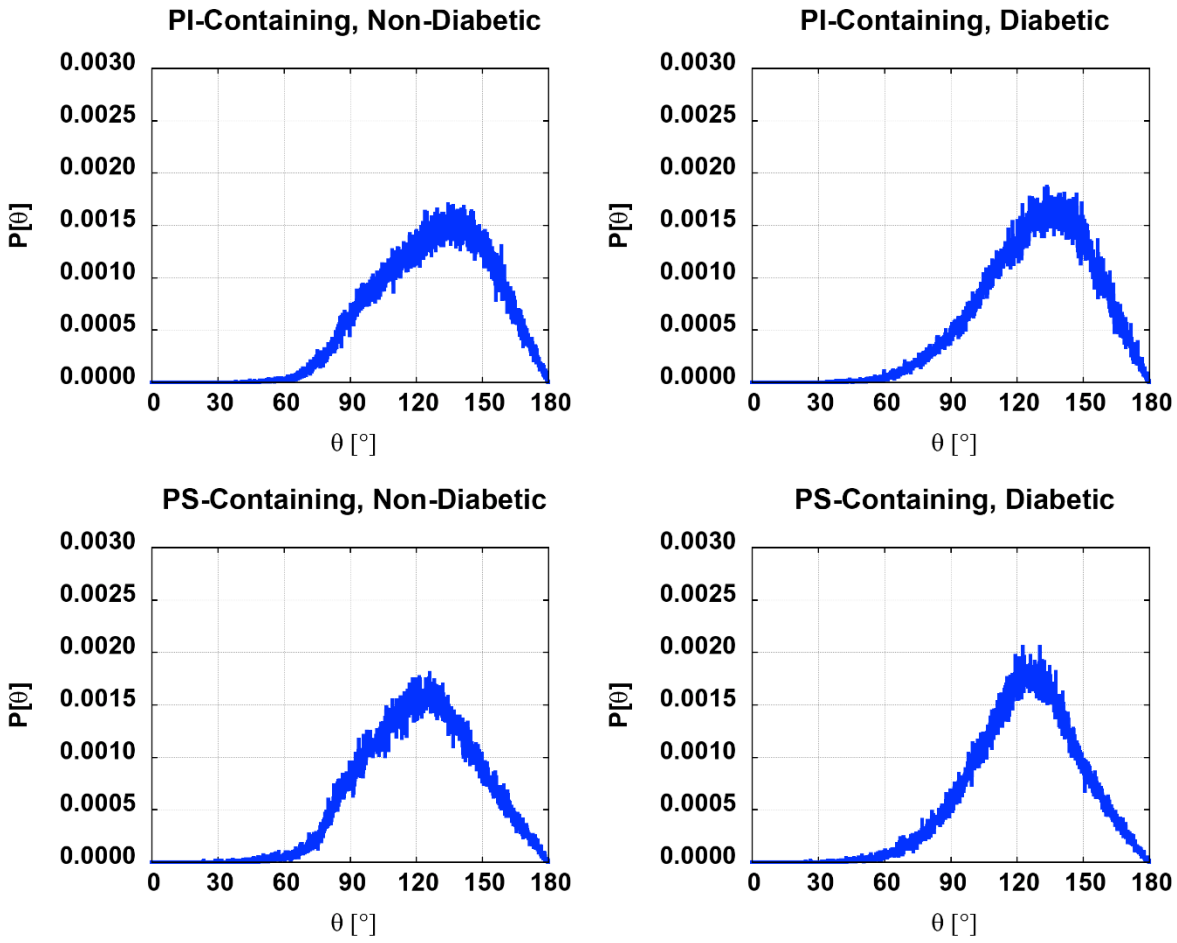

Figure 6. Average tilt angle distributions for BGAL in all model membranes with the angle defined by vector in Figure 2 relative to the bilayer normal.

3.4 Hydrogen Bonding and Two-Dimensional Radial Distribution Functions (2D-RDFs)

Hydrogen bonds, forming between lipid-lipid and lipid-cholesterol, play a crucial role in the overall organization of the lipid membrane. Both intra and inter-lipid hydrogen bonding data can be found at **Table 5**. Outside of SSM and SLPI, the other lipids have minimal intra-lipid hydrogen bonding. SSM differs from its sphingolipid counterpart GalCer in its possession of a negatively-charged phosphate group, providing more favorable interactions to its nearby amine hydrogen donor. SLPI has markedly higher intra-lipid bonding than SLPS/DOPS and PE-lipids as a result of heightened interactions between its phosphate to inositol's five hydroxyl groups compared to serine's or ethanolamine's single charged amine.

Table 5. Intra and inter-lipid hydrogen bond counts for all viable lipids. Errors are standard errors (SE) from the three replicates.

A: Intra-lipid hydrogen bonding (within the same lipid)

	Lipid	Average NHB ± SE	Average NHB/Lipid ± SE
PI-Containing, Non-Diabetic	**GalCer**	1.284 ± 0.085	0.032 ± 0.002
	SLPE	1.595 ± 0.036	0.073 ± 0.002
	SLPI	8.025 ± 0.343	0.309 ± 0.013
	SSM	8.988 ± 0.12	0.562 ± 0.008
PS-Containing, Non-Diabetic	**GalCer**	1.324 ± 0.252	0.033 ± 0.006
	DOPS	0.7 ± 0.028	0.07 ± 0.003
	SLPE	1.408 ± 0.033	0.064 ± 0.002
	SLPS	1.063 ± 0.118	0.066 ± 0.007
	SSM	8.798 ± 0.048	0.55 ± 0.003
PI-Containing, Diabetic	**GalCer**	1.579 ± 0.253	0.038 ± 0.006
	SLPE	0.9 ± 0.047	0.075 ± 0.004
	SLPI	11.392 ± 0.349	0.3 ± 0.009
	SOPE	1.163 ± 0.034	0.083 ± 0.002
	SSM	14.242 ± 0.062	0.548 ± 0.002
PS-Containing, Diabetic	**GalCer**	1.33 ± 0.067	0.032 ± 0.002
	DOPS	0.62 ± 0.035	0.062 ± 0.004
	DSPE	2.148 ± 0.062	0.067 ± 0.002
	SLPS	2.013 ± 0.063	0.072 ± 0.002
	SSM	13.102 ± 0.084	0.546 ± 0.004

B: Inter-lipid hydrogen bonding (with other lipids)

	Lipid	Average NHB ± SE	Average NHB/Lipid ± SE
PI-Containing, Non-Diabetic	**ALPC**	7.271 ± 0.317	0.727 ± 0.032
	CHL1	17.291 ± 1.204	0.24 ± 0.017
	DOPC	9.957 ± 0.497	0.711 ± 0.036
	GalCer	40.48 ± 1.239	1.012 ± 0.031
	SLPE	18.538 ± 1.133	0.843 ± 0.052
	SLPI	24.338 ± 1.284	0.936 ± 0.049
	SSM	13.753 ± 0.965	0.86 ± 0.06
PS-Containing, Non-Diabetic	**ALPC**	6.38 ± 0.535	0.532 ± 0.045
	CHL1	16.943 ± 0.575	0.229 ± 0.008
	DOPC	5.382 ± 0.419	0.538 ± 0.042
	GalCer	39.367 ± 0.776	0.984 ± 0.019
	DOPS	11.568 ± 0.573	1.157 ± 0.057
	SLPE	20.345 ± 0.604	0.925 ± 0.028

	SLPS	18.647 ± 0.977	1.165 ± 0.061
	SSM	12.698 ± 0.402	0.794 ± 0.025
PI-Containing, Diabetic	**ALPC**	8.057 ± 0.608	0.576 ± 0.043
	CHL1	7.193 ± 0.441	0.257 ± 0.016
	DSPC	15.596 ± 1.109	0.6 ± 0.043
	GalCer	48.188 ± 1.056	1.147 ± 0.025
	SLPE	10.752 ± 0.5	0.896 ± 0.042
	SLPI	34.708 ± 1.138	0.913 ± 0.03
	SOPE	12.069 ± 0.484	0.862 ± 0.035
	SSM	19.317 ± 0.711	0.743 ± 0.027
PS-Containing, Diabetic	**ALPC**	12.463 ± 0.842	0.519 ± 0.035
	CHL1	7.609 ± 0.487	0.272 ± 0.017
	DSPC	6.001 ± 0.523	0.5 ± 0.044
	GalCer	48.493 ± 1.149	1.155 ± 0.027
	DOPS	12.955 ± 0.498	1.296 ± 0.05
	DSPE	31.051 ± 0.848	0.97 ± 0.027
	SLPS	31.592 ± 1.93	1.128 ± 0.069
	SSM	15.532 ± 0.723	0.647 ± 0.03

CHL1 lacks an acceptor and as such cannot form bonds with other CHL1, so it has slightly decreased inter-lipid hydrogen bonding in non-diabetic models due to the proportionally higher CHL1 fraction compared to other lipids. GalCer also has lower inter-lipid bonding in the non-diabetic models as a result of its percentage staying relatively constant between models unlike the other sphingolipids and phospholipids, while the poorly-bonding CHL1 component increases, diminishing the amount of potential bonding sites GalCer can participate in. This aligns with the increased tilt angles seen for BGAL in diabetic models (**Figure 6**). As they have little intra-lipid hydrogen bonding and thus more free bonding sites, SLPS and DOPS have somewhat higher inter-lipid bonding compared to SLPI. PC-lipids (such as ALPC) and SSM have somewhat higher inter-lipid bonding in PI-containing models, while the reverse shows in PE-lipids (such as SLPE). PC-lipids only have a phosphate acceptor, so the donor-heavy inositol is more prone to bonding to it than serine. Likewise, SSM has utilized more of its donor sites in its heavy intra-lipid hydrogen bonding, and as such is more likely to form inter-lipid bonds through its phosphate acceptor, where inositol is again more likely to bind to than serine. Conversely, PE-lipids have low intra-lipid

bonding, resulting in free donor sites which are more likely to bind to serine, with its two additional oxygen acceptor sites on the carboxylate group, than to inositol.

The differences in hydrogen bonding demonstrated here between PI- and PS-lipids can be used to aid in explaining the previously noted differences in various properties between PI-containing and PS-containing model membranes (see previous sections). First of all, due to the significant intra-lipid hydrogen bonding present in SLPI, the inositol head tilt angle is affected by this hydrogen bond pattern. Thus, there is an unexpectedly similar (considering the stark differences in headgroup structure— refer to **Figure 2**) tilt angle distribution between PI- and PS-lipids as shown in **Figure S7**, but this is not due to equivalent molecular interactions— More of the tilt in PI-lipids is caused by intra-lipid hydrogen bonding of inositol hydroxyl groups to the phosphate, whereas more of the tilt in PS-lipids is caused by inter-lipid hydrogen bonding between serine and other lipids. Tilt induced through inter-lipid hydrogen bonding may result in a "pushing" phenomenon between lipids — the bond gives the headgroup leverage, and through the tilt itself, inter-lipid distances may be increased. From the greater inter-lipid bonding with PS-lipids, this should occur more frequently with them. Also, considering that inositol, a six-carbon ring, is larger than serine, there should also be an excluded volume factor, causing inositol to often be positioned on a somewhat higher plane than serine, which is more likely to be embedded deeper into the membrane. The cumulative result of these factors is such that the serine head of PS-lipids is producing a greater space-increasing pushing effect deeper in the membrane proper on other lipids, while the inositol head of PI-lipids is situated farther up above the membrane, with much of its tilt angle not having a spatial effect on nearby lipids. Snapshots of these occurrences can be found in **Figure 7**. As a result of this, SA/lipid (**Tables 2 and 3**) is slightly higher in PS-containing models due to increased lateral space, also aligning with the slight decreases in chain order (**Figures 3 and S4**) from the headgroup force. In addition to the simple SA/lipid modulated D_B thickness decrease in **Table 4**, the aforementioned excluded volume factor also plays a role in increasing water penetration, with the lower-situated serine headgroup more capable of drawing water molecules to a lower plane within the membrane, further decreasing D_B.

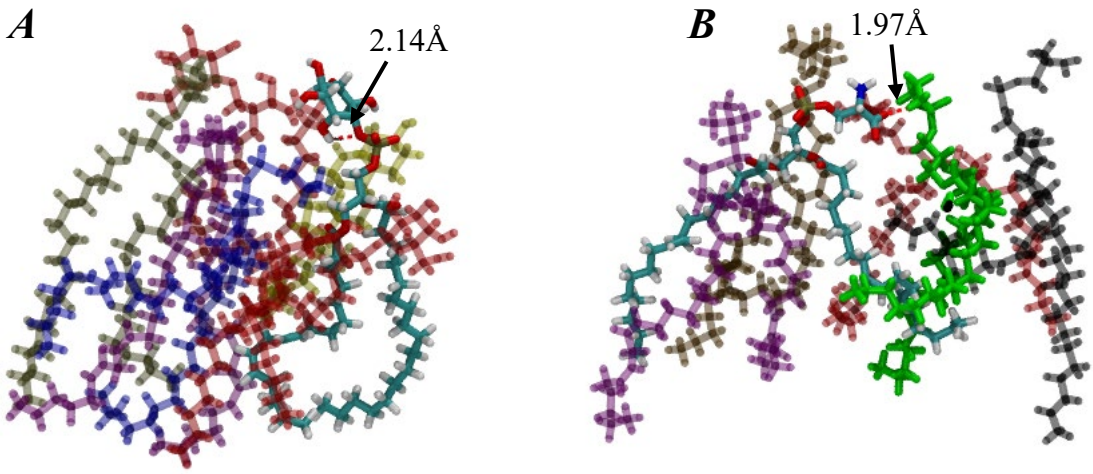

Figure 7. (**A**) shows a snapshot of SLPI (hydrogen atoms in white, oxygen in red) protruding above a cluster of lipids while forming intra-lipid hydrogen bonds (distance between atoms = 2.14 Å). (**B**) shows a snapshot of DOPS (same coloration as SLPI) at a heavily tilted angle forming an inter-lipid hydrogen bond (distance between atoms = 1.97 Å) between its oxygen and a hydrogen on a DSPE (entire lipid is colored green), while its cluster exhibits increased distance between lipids. Both are from diabetic models. Other than SLPI and DOPS, lipid color coding is the same as in **Figure 1**.

Although the differences between BGAL tilt angle distributions in diabetic and non-diabetic models can be explained simply through GalCer's heightened overall hydrogen bonding in diabetic models, specific pair data for CER160 only (not including the O1 oxygen, which is considered part of BGAL— see **Figure 2**) is needed to explain differences between the PI-containing and PS-containing models. **Table 6** shows the total amount of specific pairing between CER160 and PI/PS-lipids. Here, it is visible that CER160 bonds more often with PI-lipids than PS-lipids, which is counterintuitive in that it contains more donor sites than acceptor sites and in this should be able to form more bonds to the acceptor-heavy serine. However, BGAL is a large headgroup similar in size to inositol and may more frequently protrude above other headgroups as well from excluded volume. This similarity in position would lead to more hydrogen bonding with PI-lipids, which results in a more bound-in-place GalCer, and a somewhat greater angle required in BGAL for it to form hydrogen bonds with other lipids on a lower plane.

Table 6. Counts for hydrogen bonds formed between CER160 and all PI or PS-lipids. Errors are standard errors (SE) from the three replicates.

	PI-Containing, Non-Diabetic	**PI-Containing, Diabetic**	**PS-Containing, Non-Diabetic**	**PS-Containing, Diabetic**
Total bonds between CER160 and PI/PS-lipids ± SE	2.870 ± 0.220	3.207 ± 0.744	1.330 ± 0.301	1.606 ± 0.262

2D-RDF's can additionally help demonstrate how different lipid types assemble into structures within the membrane. Sample figures for various lipids and cholesterol are provided in **Figure S8** and **8**, respectively, with cross-model differences mostly aligning to trends in hydrogen bonding. PE-PS has stronger peaks than PE-PI between radial distances of 5 and 10 Å, which can be attributed to the former's higher inter-lipid hydrogen bonding. Likewise, PC-PI has visibly stronger peaks than PC-PS in the same area. PI-CER experiences peaks at radial distances of 5 Å which are not present in PS-CER, also following the increased hydrogen bonding trend noted. In the non-diabetic CHL1-CHL1 2D-RDF's, there is greater long-range order past the first peak, with the third and fourth peaks separated equidistantly. This suggests an ordered, linear assembly pattern of cholesterol, indicating greater packing and aligning with their overall higher content. The diabetic models do not exhibit this, indicating greater membrane fluidity, and also contain a stronger first peak (at radial distance ~6-7 Å), suggesting an increase in the first solvation shell and segregation from other lipids. For all non-diabetic 2D-RDF's, variation is small between triplicates, indicating good convergence within this property. It is noted, however, that these CHL1-CHL1 diabetic figures also exhibit some degree of variance, which may be attributed to some remaining dependency on the starting structure. However, this should not be a concern for the purposes of analysis as the three replicas taken together should represent an approximation to the ensemble average.

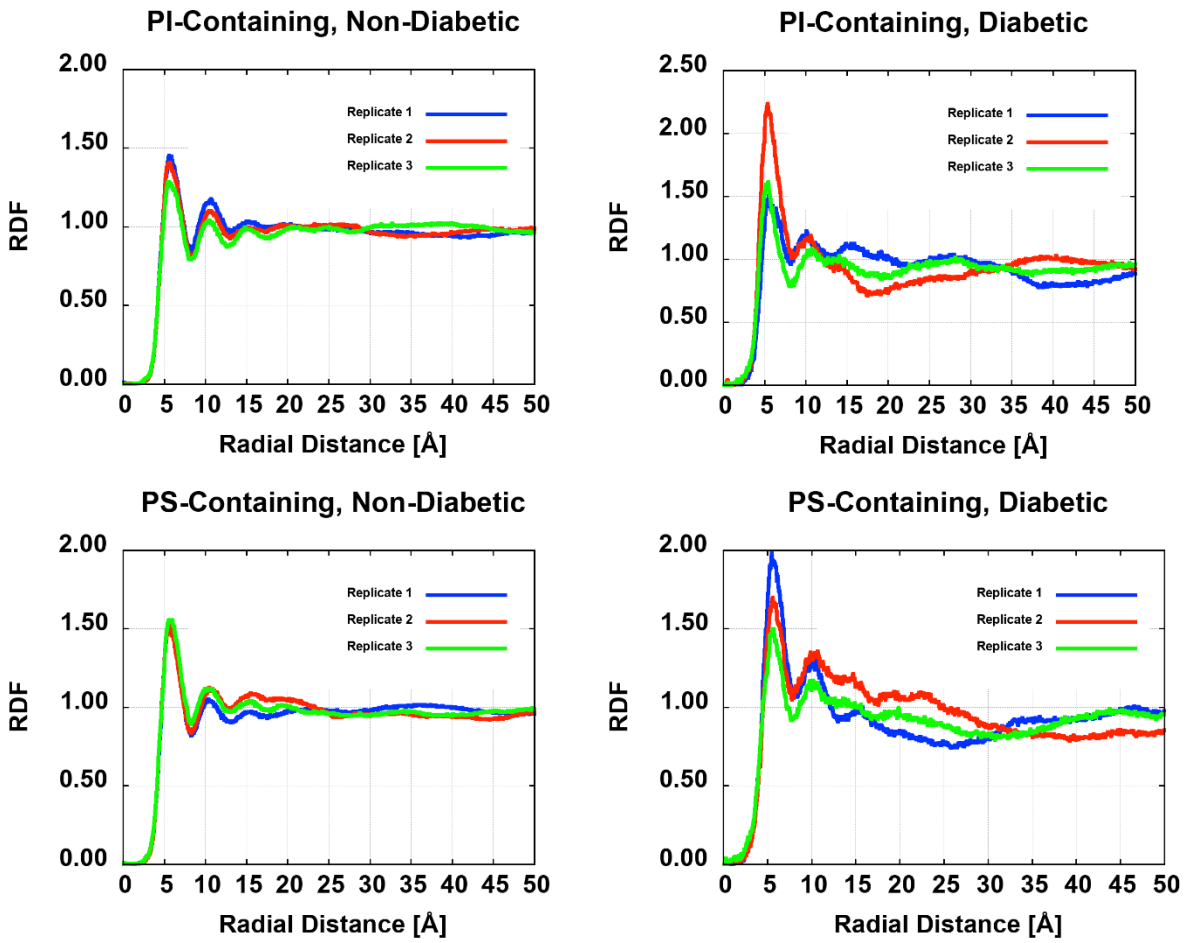

Figure 8. CHL1-CHL1 2D-RDF's

4. Discussion and Conclusions

Through the use of MD with the CHARMM36 lipid force field, we have modeled and simulated the myelin sheath of rat sciatic nerves in four conditions—PI-containing (non-diabetic and diabetic) and PS-containing (non-diabetic and diabetic), all fully hydrated and at a physiological condition of 37 °C. Simulations were run in triplicates with different initial lipid placements for 400ns and 600ns for the diabetic and non-diabetic models respectively, with all models reaching equilibration and convergence in SA/lipid prior to the final 150ns. Between the diabetic and non-diabetic membranes, the most notable differences are that diabetic membranes have significantly lower cholesterol and lower unsaturated fatty acid content, which may be attributed to the lowered expression of fatty acid synthesis-related genes and levels of sterol-regulatory element binding factor-1c.[15-16] PI-containing membranes contain 13 and 19% PI-lipid

for non-diabetic and diabetic membranes respectively, with no PS-lipid inclusion. The reverse is true for PS-containing membranes. Outside of these, differences between the model membranes are minimal and unlikely to cause major changes in membrane properties.

It is noted that there are limitations to our approach regarding bilayer accuracy and simulation timescale. Although individual leaflet compositions were not provided in the main experimental study used, in older studies on mammalian peripheral nerve myelin membranes, a degree of asymmetry has been detected.[15, 25] In particular, in isolated and unfolded myelin, ceramides (such as GalCer) were found to be heavily localized to the extracellular leaflet, with small asymmetries in phospholipids as well.[50-51] In intact folded myelin, asymmetries have been detected as well, but the scope of these studies has been more limited and currently, there is little information on potential differences in asymmetry throughout myelin lamellae *in-vivo*.[52] Nevertheless, it is likely that there is some degree of overall asymmetry in myelin, which is most prominent in ceramide distribution. Overall, our current models should supply reasonable conclusions, especially regarding the ceramide-heavy extracellular leaflet, and as such a good starting point, but even more complex and realistic myelin membranes, incorporating asymmetry, multiple layers, membrane proteins, and/or gangliosides, could be probed in future studies. With regards to simulation time, increased timescale lengths could result in more polished convergence in the 2D-RDF's, as well as the ability to sample additional membrane properties. However, the converged triplicate simulations should be sufficient for an approximation to the ensemble average, and thus the current membrane property analyses.

There are several significant changes in membrane properties going from non-diabetic to diabetic, all which can be explained through the lowered cholesterol content. As seen in **Table 2**, the overall SA/lipid is much higher in both diabetic models, and the K_A is much lower, which correspond to lower packing from a lower fraction of rigid cholesterol components. This pattern extends to the component SA/lipid in **Table 3**, as well as the generally decreased S_{CD} in **Figures 3 and S4**. As a result of the decreased lateral packing shown through SA/lipid, lipids are laterally more spread out, and less vertically rigid, leading to decreased vertical thicknesses (see **Table 4**). Also stemming from the increased inter-lipid spacing, **Figure S7**'s tilt angles show that cholesterol is less vertical in diabetic membranes. Finally, the diabetic 2D-RDF's in **Figure 8** possess stronger first peaks and decreased long-range order compared to their non-diabetic counterparts, showing overall greater membrane fluidity and segregation from other lipids. These changes are reversed

from the more ordered bilayer expected from the concurrent decreases in unsaturated fatty acid content, suggesting cholesterol precedence here as a driver in disease state membrane properties.

Structurally, these changes in the diabetic condition result in a thinner, more spread-out, and less rigid membrane modulated by decreases in cholesterol content. In an earlier electron spin resonance spectroscopy study, Zuvic-Butorac et al.[53] reported an increased fluidity in diabetic rat sciatic nerve myelin, suggesting that it could stem simply from changes in lipid composition. As the only differences between the models were in lipid composition, our results agree well with this. These results also correspond well to reports of myelin sheath damage and atrophy prior to the onset of diabetic peripheral neuropathy (DPN), as thinner, less tightly packed, and more fluid membranes are logically more likely to suffer damage.[13-14] Overall, our results provide further evidence for the direct role of lipid composition changes in causing diabetic myelin weakness and damage, ultimately contributing to DPN.

Alternating PS and PI-lipids in the model membranes also result in property differences, although generally more subtle than between non-diabetic and diabetic compositions. As shown through hydrogen bonding differences in **Table 5**, PI-lipids experience overall more intra-lipid bonding due to their stronger and more numerous hydrogen bond donors (hydroxyl groups on the inositol carbon ring), while PS-lipids experience comparatively more inter-lipid bonding. Within inter-lipid bonding, PI-lipids are more likely to form bonds with SM and PC-lipids, while PS-lipids are more likely to form bonds with PE-lipids. Inositol is also larger than serine and will more likely be protruding to a higher plane from the main membrane due to excluded volume, while serine is more likely to be found deeper within the main membrane. As a result, despite their similar tilt angles (**Figure S7**), more of the PS tilt should be pushing on other lipids in the membrane proper, while more of the PI tilt should be due to binding with itself somewhat higher above the membrane proper, having slightly less spatial effect on surrounding lipids (**Figure 7** shows a snapshot). This accounts for the slightly increased SA/lipid (**Tables 2 and 3**) and decreased chain order (**Figures 3 and S4**) in PS-containing models, as well as the lower D_B (water) thicknesses (**Table 4**), which result from a combination of the increased SA/lipid allowing more water in and simply the PS headgroup drawing more water molecules to a lower plane.

As a whole, higher PS-lipid content results in a slightly more spread-out, less rigid membrane, while higher PI-lipid content has a somewhat lesser effect on structural properties due to its outwards protrusion and higher proportion of intra-lipid hydrogen bonding. These

phenomena have interesting possible implications for PI and PS-related biological processes. Phosphorylated PI-lipids, or phosphoinositides, play a multitude of important roles in cell signaling, notably phosphatidylinositol 4,5-biphosphate, which is hydrolyzed by phospholipase C (PLC) enzymes to produce the second messengers 1,4,5-triphosphate (Ip3) and diacylglycerol (DAG).[20, 22] In order for a PI-lipid to become a phosphoinositide, however, it must be phosphorylated by signal transducer enzymes such as PI3K, which would need access to its headgroup.[22] The relative outward protrusion of PI-lipids due to excluded volume may aid enzymes in phosphorylating the inositol headgroup. Normally, PC and SM-lipids *in vivo* are more frequent on the outer leaflet, opposite of PI, but in the case an enzyme such as ATP10A PC flippase has abnormal activity, there is the possibility for high PC and SM-lipid content on the inner leaflet, neighboring PI.[54-55] Due to the higher chances of PI-lipids forming hydrogen bonds with these, access to enzymes may become slightly more limited in such a situation, possibly diminishing phosphoinositide production. Also, it was shown that asymmetries in surface area between inner and outer leaflets resulted in endocytic vesicle formation through an increase in membrane curvature.[56] As PS is positioned primarily on the cytosolic leaflet of lipid membrane, its surface area-increasing activity demonstrated here could have important consequences on the vesicle budding process.[21] Further research could focus more deeply on PI-lipid biophysics, analyzing if membrane organizational factors could lead to perturbations of phosphorylation, as well as into the effects of inner leaflet PS composition abnormalities on the ability of cells to form endocytic vesicles. Finally, an earlier simulation study by Wu et al.[57] analyzed the height and tilt angle of phosphoinositides in lipid membranes consisting primarily of either PC or PS-lipids, where it was found that phosphoinositides had slightly lower *Z*-axis protrusion from the surface in membranes with PS-lipids as a primary component, matching well with what we have described here. Due to the inter-lipid distance-increasing property of PS-lipids relative to PC, phosphoinositide headgroups should be more prone towards sinking deeper in the membrane itself in primarily PS-lipid membranes.

Both disease conditions and PI vs. PS-lipid content affected the orientation of the BGAL headgroup in GalCer, but the former produced a more notable change, as shown in **Figure 6**. In diabetic membranes, BGAL is tilted further away from the membrane normal as a result of proportionally increased phospholipid content and inter-lipid hydrogen bonding. “Sugar zippers”, or apposing membrane leaflets held together through cholesterol interactions, may play a strong

role in the stability of multilayered membranes such as the myelin sheath.[58-59] In diabetic membranes, the increased inter-lipid hydrogen bonding and less vertical headgroup may result in less hydrogen bonding potential with apposing GalCer, leading to greater myelin instability on top of the already weakened bilayers, making myelin deterioration even more likely. Further research could be done on multilayered myelin sheath models to investigate such effects.

Two of the calculated properties, S_{CD} and D_{HH}, were compared to experimental data. In **Figure 4**, the S_{CD} profiles of the GalCer 18:1 chain in all models is compared to that of GalCer 18:0 chains in an experimental 7% GalCer, 70% SOPC, and 23% cholesterol membrane, where it is seen that the experimental profiles align with the non-diabetic 18:1 profiles.[46] This is the expected result considering that both non-diabetic and experimental membranes are above ~20% cholesterol and thus in the liquid-ordered (L_o) state, which should induce similar chain orders, demonstrating agreement between experiment and simulation. Experimental headgroup-to-headgroup (D_{HH}) thicknesses of rat sciatic nerve myelin bilayers are 47.0 ± 2.0 Å, which is close to the 43.3 ± 0.2 Å and 43.5 ± 0.2 Å thicknesses for the respective PI and PS-containing non-diabetic membranes if a ~1-4 Å thickness decrease for temperature differences is taken into account.[48-49]

In conclusion, as a result of decreases in cholesterol, diabetic models have a more laterally expansive, thinner, and less rigid membrane, which is more prone to atrophy and damage, providing evidence for the role of lipid composition changes in inducing diabetic peripheral neuropathy. This is compounded with a potential reduction in the ability of GalCer to interact with its counterparts on opposing membranes, which may cause weaknesses in the multilayered structure of the myelin sheath. The inclusion of PS-lipids was found to lead to increased inter-lipid spacing and decreased order within membranes, which is likely due to some degree of a headgroup pushing effect within the membrane as a result of the comparatively small serine not protruding out of the membrane, and high inter-lipid hydrogen bonding ability. In contrast, the lesser effect of PI-lipid inclusion is likely due to their larger headgroup and proportionally higher intra-lipid hydrogen bonding ability, leading to more frequent protrusion above the membrane and less attachment and pushing effect on other lipids. Comparisons of GalCer S_{CD} profiles and non-diabetic D_{HH} show close alignment to available experimental data, supporting both the applicability of these conclusions as well as the usage of the complex rat sciatic nerve myelin sheath models simulated and analyzed here in future simulation studies, which could probe PNS

myelin in greater complexity, including bilayer asymmetries, multiple layers, and other crucial components for its structure and function.

Supporting Information

Additional figures and tables on membrane properties, as well as simulation movie files, are presented in the supplementary materials section.

Acknowledgements

The high-performance computational resources used for this research are Deepthought2 and Bluecrab, maintained by the Division of Information Technology at the University of Maryland and the Maryland Advanced Research Computing Center (MARCC) respectively. This research was supported in part by NSF (CHE-2003912) and the NIH intramural program (Yalun Yu).

References

1. Morell, P.; Quarles, R. H., The Myelin Sheath. In *Basic Neurochemistry: Molecular, Cellular and Medical Aspects*, 6 ed.; Siegel, G. J.; Agranoff, B. W.; Albers, W.; Fisher, S. K.; Uhler, M. D., Eds. Lipincott-Raven: Philadelphia, 1999.
2. Taveggia, C.; Feltri, M. L.; Wrabetz, L., Signals to promote myelin formation and repair. *Nat Rev Neurol* **2010,** *6* (5), 276-87.
3. Bogdanov, M.; Heacock, P.; Guan, Z.; Dowhan, W., Plasticity of lipid-protein interactions in the function and topogenesis of the membrane protein lactose permease from Escherichia coli. *Proceedings of the National Academy of Sciences* **2010,** *107* (34), 15057-15062.
4. van Meer, G.; Voelker, D. R.; Feigenson, G. W., Membrane lipids: where they are and how they behave. *Nat Rev Mol Cell Biol* **2008,** *9* (2), 112-24.
5. Maxfield, F. R.; Tabas, I., Role of cholesterol and lipid organization in disease. *Nature* **2005,** *438* (7068), 612-621.
6. Bosio, A.; Binczek, E.; Haupt, W. F.; Stoffel, W., Composition and biophysical properties of myelin lipid define the neurological defects in galactocerebroside- and sulfatide-deficient mice. *J Neurochem* **1998,** *70* (1), 308-15.
7. Monje-Galvan, V.; Klauda, J. B., Modeling Yeast Organelle Membranes and How Lipid Diversity Influences Bilayer Properties. *Biochemistry* **2015,** *54* (45), 6852-61.
8. Pandit, K. R.; Klauda, J. B., Membrane models of E. coli containing cyclic moieties in the aliphatic lipid chain. *Biochim Biophys Acta* **2012,** *1818* (5), 1205-10.
9. Zhuang, X.; Ou, A.; Klauda, J. B., Simulations of simple linoleic acid-containing lipid membranes and models for the soybean plasma membranes. *J Chem Phys* **2017,** *146* (21), 215103.
10. Yu, Y.; Klauda, J. B., Modeling Pseudomonas aeruginosa inner plasma membrane in planktonic and biofilm modes. *J Chem Phys* **2018,** *149* (21), 215102.
11. Schyboll, F.; Jaekel, U.; Petruccione, F.; Neeb, H., Dipolar induced spin-lattice relaxation in the myelin sheath: A molecular dynamics study. *Scientific Reports* **2019,** *9* (1), 14813.
12. Li, K.; Shi, X.; Luo, M.; Inam, U. L.; Wu, P.; Zhang, M.; Zhang, C.; Li, Q.; Wang, Y.; Piao, F., Taurine protects against myelin damage of sciatic nerve in diabetic peripheral neuropathy rats by controlling apoptosis of schwann cells via NGF/Akt/GSK3β pathway. *Exp Cell Res* **2019,** *383* (2), 111557.
13. Sinnreich, M.; Taylor, B. V.; Dyck, P. J., Diabetic neuropathies. Classification, clinical features, and pathophysiological basis. *Neurologist* **2005,** *11* (2), 63-79.
14. Sugimoto, K.; Murakawa, Y.; Sima, A. A. F., Diabetic neuropathy – a continuing enigma. *Diabetes/Metabolism Research and Reviews* **2000,** *16* (6), 408-433.
15. Cermenati, G.; Abbiati, F.; Cermenati, S.; Brioschi, E.; Volonterio, A.; Cavaletti, G.; Saez, E.; De Fabiani, E.; Crestani, M.; Garcia-Segura, L. M.; Melcangi, R. C.; Caruso, D.; Mitro, N., Diabetes-induced myelin abnormalities are associated with an altered lipid pattern: protective effects of LXR activation. *Journal of Lipid Research* **2012,** *53* (2), 300-310.
16. de Preux, A. S.; Goosen, K.; Zhang, W.; Sima, A. A.; Shimano, H.; Ouwens, D. M.; Diamant, M.; Hillebrands, J. L.; Rozing, J.; Lemke, G.; Beckmann, J. S.; Smit, A. B.; Verheijen, M. H.; Chrast, R., SREBP-1c expression in Schwann cells is affected by diabetes and nutritional status. *Mol Cell Neurosci* **2007,** *35* (4), 525-34.

17. Smith, M. E.; Curtis, B. M., FROG SCIATIC NERVE MYELIN: A CHEMICAL CHARACTERIZATION. *Journal of Neurochemistry* **1979,** *33* (2), 447-452.
18. Evans, M. J.; Finean, J. B., The lipid composition of myelin from brain and peripheral nerve. *Journal of Neurochemistry* **1965,** *12* (8), 729-734.
19. Svennerholm, L.; Boström, K.; Fredman, P.; Jungbjer, B.; Månsson, J. E.; Rynmark, B. M., Membrane lipids of human peripheral nerve and spinal cord. *Biochim Biophys Acta* **1992,** *1128* (1), 1-7.
20. Zhu, L.; Jones, C.; Zhang, G., The Role of Phospholipase C Signaling in Macrophage-Mediated Inflammatory Response. *Journal of Immunology Research* **2018,** *2018*, 5201759.
21. Leventis, P. A.; Grinstein, S., The distribution and function of phosphatidylserine in cellular membranes. *Annu Rev Biophys* **2010,** *39*, 407-27.
22. Balla, T., Phosphoinositides: tiny lipids with giant impact on cell regulation. *Physiol Rev* **2013,** *93* (3), 1019-137.
23. Lees, M. B.; Brostoff, S. W., Proteins of myelin. In *Myelin*, 2 ed.; Morell, P., Ed. Plenum: New York, 1984; pp 197-217.
24. Ogawa-Goto, K.; Funamoto, N.; Ohta, Y.; Abe, T.; Nagashima, K., Myelin gangliosides of human peripheral nervous system: an enrichment of GM1 in the motor nerve myelin isolated from cauda equina. *J Neurochem* **1992,** *59* (5), 1844-9.
25. Inouye, H.; Kirschner, D. A., Membrane interactions in nerve myelin: II. Determination of surface charge from biochemical data. *Biophysical Journal* **1988,** *53* (2), 247-260.
26. Jeon, S.-B.; Yoon, H. J.; Park, S.-H.; Kim, I.-H.; Park, E. J., Sulfatide, A Major Lipid Component of Myelin Sheath, Activates Inflammatory Responses As an Endogenous Stimulator in Brain-Resident Immune Cells. *The Journal of Immunology* **2008,** *181* (11), 8077.
27. Jo, S.; Lim, J. B.; Klauda, J. B.; Im, W., CHARMM-GUI Membrane Builder for mixed bilayers and its application to yeast membranes. *Biophysical journal* **2009,** *97* (1), 50-58.
28. Jo, S.; Kim, T.; Im, W., Automated builder and database of protein/membrane complexes for molecular dynamics simulations. *PloS one* **2007,** *2* (9), e880-e880.
29. Jo, S.; Kim, T.; Iyer, V. G.; Im, W., CHARMM-GUI: a web-based graphical user interface for CHARMM. *J Comput Chem* **2008,** *29* (11), 1859-65.
30. Wu, E. L.; Cheng, X.; Jo, S.; Rui, H.; Song, K. C.; Dávila-Contreras, E. M.; Qi, Y.; Lee, J.; Monje-Galvan, V.; Venable, R. M.; Klauda, J. B.; Im, W., CHARMM-GUI Membrane Builder toward realistic biological membrane simulations. *J Comput Chem* **2014,** *35* (27), 1997-2004.
31. Phillips, J. C.; Braun, R.; Wang, W.; Gumbart, J.; Tajkhorshid, E.; Villa, E.; Chipot, C.; Skeel, R. D.; Kalé, L.; Schulten, K., Scalable molecular dynamics with NAMD. *Journal of Computational Chemistry* **2005,** *26* (16), 1781-1802.
32. Klauda, J. B.; Venable, R. M.; Freites, J. A.; O'Connor, J. W.; Tobias, D. J.; Mondragon-Ramirez, C.; Vorobyov, I.; MacKerell, A. D.; Pastor, R. W., Update of the CHARMM All-Atom Additive Force Field for Lipids: Validation on Six Lipid Types. *The Journal of Physical Chemistry B* **2010,** *114* (23), 7830-7843.
33. Durell, S. R.; Brooks, B. R.; Ben-Naim, A., Solvent-Induced Forces between Two Hydrophilic Groups. *The Journal of Physical Chemistry* **1994,** *98* (8), 2198-2202.
34. Jorgensen, W. L.; Chandrasekhar, J.; Madura, J. D.; Impey, R. W.; Klein, M. L., Comparison of simple potential functions for simulating liquid water. *The Journal of Chemical Physics* **1983,** *79* (2), 926-935.

35. Lillie, L. E.; Temple, N. J.; Florence, L. Z., Reference values for young normal Sprague-Dawley rats: weight gain, hematology and clinical chemistry. *Hum Exp Toxicol* **1996,** *15* (8), 612-6.
36. Feller, S. E.; Zhang, Y.; Pastor, R. W.; Brooks, B. R., Constant pressure molecular dynamics simulation: The Langevin piston method. *The Journal of Chemical Physics* **1995,** *103* (11), 4613-4621.
37. Martyna, G. J.; Tobias, D. J.; Klein, M. L., Constant pressure molecular dynamics algorithms. *The Journal of Chemical Physics* **1994,** *101* (5), 4177-4189.
38. Ryckaert, J.-P.; Ciccotti, G.; Berendsen, H. J. C., Numerical integration of the cartesian equations of motion of a system with constraints: molecular dynamics of n-alkanes. *Journal of Computational Physics* **1977,** *23* (3), 327-341.
39. Darden, T.; York, D.; Pedersen, L., Particle mesh Ewald: An N·log(N) method for Ewald sums in large systems. *The Journal of Chemical Physics* **1993,** *98* (12), 10089-10092.
40. Steinbach, P. J.; Brooks, B. R., New spherical-cutoff methods for long-range forces in macromolecular simulation. *Journal of Computational Chemistry* **1994,** *15* (7), 667-683.
41. Humphrey, W.; Dalke, A.; Schulten, K., VMD: visual molecular dynamics. *J Mol Graph* **1996,** *14* (1), 33-8, 27-8.
42. MATLAB. 2020; Vol. R2019b.
43. Rohatgi, A. *WebPlotDigitizer*, 4.4; Pacifica, California, 2020.
44. Barber, C. B.; Dobkin, D. P.; Huhdanpaa, H., The quickhull algorithm for convex hulls. *ACM Trans. Math. Softw.* **1996,** *22* (4), 469–483.
45. Das, C.; Noro, M. G.; Olmsted, P. D., Simulation Studies of Stratum Corneum Lipid Mixtures. *Biophysical Journal* **2009,** *97* (7), 1941-1951.
46. Morrow, M. R.; Singh, D.; Lu, D.; Grant, C. W., Glycosphingolipid fatty acid arrangement in phospholipid bilayers: cholesterol effects. *Biophys J* **1995,** *68* (1), 179-86.
47. Hjort Ipsen, J.; Karlström, G.; Mourtisen, O. G.; Wennerström, H.; Zuckermann, M. J., Phase equilibria in the phosphatidylcholine-cholesterol system. *Biochimica et Biophysica Acta (BBA) - Biomembranes* **1987,** *905* (1), 162-172.
48. Vonasek, E.; Moran, O.; Mateu, L., An X-ray diffraction study of changes in myelin structure during experimental allergic neuritis. *J Neurocytol* **1987,** *16* (1), 105-14.
49. Zhuang, X.; Dávila-Contreras, E. M.; Beaven, A. H.; Im, W.; Klauda, J. B., An extensive simulation study of lipid bilayer properties with different head groups, acyl chain lengths, and chain saturations. *Biochimica et Biophysica Acta (BBA) - Biomembranes* **2016,** *1858* (12), 3093-3104.
50. Gwarsha, K.; Rumsby, M. G.; Little, C., On the disposition of phospholipids in freshly isolated myelin sheath preparations from bovine brain. *Neurochemistry International* **1984,** *6* (4), 599-606.
51. Linington, C.; Rumsby, M. G., Accessibility of galactosyl ceramides to probe reagents in central nervous system myelin. *J Neurochem* **1980,** *35* (4), 983-92.
52. Kirschner, D. A.; Ganser, A. L., Myelin labeled with mercuric chloride. Asymmetric localization of phosphatidylethanolamine plasmalogen. *J Mol Biol* **1982,** *157* (4), 635-58.
53. Zuvic-Butorac, M.; Kriz, J.; Simonic, A.; Schara, M., Fluidity of the myelin sheath in the peripheral nerves of diabetic rats. *Biochimica et Biophysica Acta (BBA) - Molecular Basis of Disease* **2001,** *1537* (2), 110-116.

54. Ye, W.; Han, T. W.; Nassar, L. M.; Zubia, M.; Jan, Y. N.; Jan, L. Y., Phosphatidylinositol-(4, 5)-bisphosphate regulates calcium gating of small-conductance cation channel TMEM16F. *Proceedings of the National Academy of Sciences* **2018,** *115* (7), E1667.
55. Naito, T.; Takatsu, H.; Miyano, R.; Takada, N.; Nakayama, K.; Shin, H. W., Phospholipid Flippase ATP10A Translocates Phosphatidylcholine and Is Involved in Plasma Membrane Dynamics. *J Biol Chem* **2015,** *290* (24), 15004-17.
56. Farge, E., Increased vesicle endocytosis due to an increase in the plasma membrane phosphatidylserine concentration. *Biophysical Journal* **1995,** *69* (6), 2501-2506.
57. Wu, E. L.; Qi Y Fau - Song, K. C.; Song Kc Fau - Klauda, J. B.; Klauda Jb Fau - Im, W.; Im, W., Preferred orientations of phosphoinositides in bilayers and their implications in protein recognition mechanisms. (1520-5207 (Electronic)).
58. Spillmann, D., Carbohydrates in cellular recognition: from leucine-zipper to sugar-zipper? *Glycoconjugate journal* **1994,** *11* (3), 169-171.
59. Boggs, J. M.; Menikh, A.; Rangaraj, G., Trans interactions between galactosylceramide and cerebroside sulfate across apposed bilayers. *Biophysical journal* **2000,** *78* (2), 874-885.

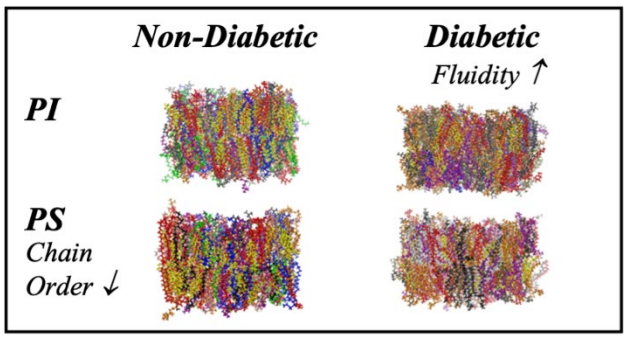

TOC Graphic.